

Highly Hydrated Paramagnetic Amorphous Calcium Carbonate Nanoclusters as a Superior MRI Contrast Agent

Liang Dong

University of Science and Technology of China

Yun-Jun Xu

The First Affiliated Hospital of University of Science and Technology of China

Cong Sui

University of Science and Technology of China

Yang Zhao

University of Science and Technology of China

Li-Bo Mao

University of Science and Technology of China <https://orcid.org/0000-0002-9249-2449>

Denis Gebauer

University of Hannover <https://orcid.org/0000-0003-1612-051X>

Rose Rosenberg

University of Konstanz

Jonathan Avaro

Empa - Swiss Federal Laboratories for Materials Science and Technology

Ya-Dong Wu

Hefei University of Technology

Huai-Ling Gao

University of Science and Technology of China <https://orcid.org/0000-0001-8908-1967>

Zhao Pan

University of Science and Technology of China

Hui-Qin Wen

The First Affiliated Hospital of Anhui Medical University

Xu Yan

Hefei University of Technology

Fei Li

Hefei University of Technology

Yang Lu

Hefei University of Technology <https://orcid.org/0000-0002-8412-809X>

Helmut Coelfen

University of Konstanz <https://orcid.org/0000-0002-1148-0308>

Shu-Hong Yu (✉ shyu@ustc.edu.cn)

University of Science and Technology of China <https://orcid.org/0000-0003-3732-1011>

Article

Keywords: amorphous calcium carbonate (ACC), MRI contrast agent, nanoclusters

Posted Date: June 11th, 2021

DOI: <https://doi.org/10.21203/rs.3.rs-598198/v1>

License: © ⓘ This work is licensed under a Creative Commons Attribution 4.0 International License.

[Read Full License](#)

Version of Record: A version of this preprint was published at Nature Communications on August 29th, 2022. See the published version at <https://doi.org/10.1038/s41467-022-32615-3>.

Highly Hydrated Paramagnetic Amorphous Calcium Carbonate Nanoclusters as a Superior MRI Contrast Agent

Liang Dong^{1*}, Yun-Jun Xu^{3*}, Cong Sui^{1*}, Yang Zhao¹, Li-Bo Mao¹, Denis Gebauer⁴, Rose Rosenberg⁵, Jonathan Avaro⁶, Ya-Dong Wu², Huai-Ling Gao¹, Zhao Pan¹, Hui-Qin Wen⁷, Xu Yan², Fei Li², Yang Lu², Helmut Cölfen⁵, Shu-Hong Yu^{1,2}

¹ Division of Nanomaterials & Chemistry, Hefei National Laboratory for Physical Sciences at the Microscale, Institute of Energy, Hefei Comprehensive National Science Center, CAS Center for Excellence in Nanoscience, Department of Chemistry, Institute of Biomimetic Materials & Chemistry, Anhui Engineering Laboratory of Biomimetic Materials, University of Science and Technology of China, Hefei 230026, China.

² School of Chemistry and Chemical Engineering, Hefei University of Technology, Hefei, 230009, China.

³ Department of Radiology, Anhui Provincial Hospital, The First Affiliated Hospital of University of Science and Technology of China, Hefei, 230001, China.

⁴ Institute of Inorganic Chemistry, Leibniz Universität Hannover, Callinstr. 9, 30167, Hannover, Germany.

⁵ Physical Chemistry, Department of Chemistry, University of Konstanz, Universitätsstr. 10, Konstanz, D-78457, Germany.

1 ⁶ *Scientist - Center for X-ray Analytics, Empa - Swiss Federal Laboratories for Materials Science and*
2 *Technology, Lerchenfeldstrasse 5, 9014, St. Gallen, Switzerland.*

3 ⁷ *Department of Blood Transfusion, The First Affiliated Hospital of Anhui Medical University, Hefei,*
4 *230022, China.*

5 * These authors contributed equally to this work.

6 Correspondence and requests for materials should be addressed to the author: Yang Lu
7 (yanglu@hfut.edu.cn), Helmut Cölfen (helmut.coelfen@uni-konstanz.de) or Shu-Hong Yu
8 (shyu@ustc.edu.cn).

9

1 **Abstract**

2 Amorphous calcium carbonate (ACC) plays a key role as transient precursor in the early stages of biogenic
3 calcium carbonate formation in nature. However, due to its instability in aqueous solution, there is still
4 rare success to utilize ACC in biomedicine. Here, we report the mutual effect between paramagnetic
5 gadolinium ions and ACC, resulting in ultrafine paramagnetic amorphous carbonate nanoclusters (ACNC)
6 in the presence of both gadolinium occluded highly hydrated ACC-like environment and poly(acrylic acid).
7 Gadolinium is confirmed to enhance the water content in ACC, and the high water content of ACNC (23
8 molecules H₂O per 1 Gd) contributes to the much enhanced magnetic resonance imaging (MRI) contrast
9 efficiency compared with commercially available gadolinium-based contrast agents. Furthermore, the
10 enhanced T_1 weighted MRI performance and biocompatibility of ACNC are further evaluated in various
11 animals including rat, rabbit and beagle dog, in combination with promising safety *in vivo*. Overall,
12 exceptionally facile mass-productive ACNC exhibits superb imaging performance and impressive stability,
13 which provides a promising strategy to design MR contrast agents.

1 Introduction

2 Amorphous calcium carbonate (ACC), which exists widely in nature, plays a key role as transient
3 precursor in the early stages of biomineral formation¹⁻⁴. Using a bioinspired strategy, diverse materials
4 with controlled phase, physical and chemical properties can be achieved^{5, 6}. The highly hydrated content
5 is a distinctive feature of ACC, and plays a pivotal role in its stabilization⁶⁻¹². As a metastable phase of
6 calcium carbonate, ACC is unstable in aqueous solution and will transform into crystalline phases rapidly
7 owing to dehydration, ion binding and other factors^{6-8, 13}. Therefore, the potential application of highly
8 hydrated ACC is largely ignored, and there are few successful examples to utilize ACC in biomedicine.

9 One significant parameter to enhance the contrasting performance of gadolinium-based T_1 MRI contrast
10 agents is their hydration¹⁴. With seven non-paired electrons, the gadolinium ion possesses a large magnetic
11 moment and long electron spin relaxation time, leading to numerous clinically available extracellular
12 gadolinium-based contrast agents for T_1 MRI^{14, 15}. In virtue of versatile functionalization to interact with
13 biomolecules *in vivo* and lower gadolinium ion leakage rates benefitting from an inorganic nanostructure,
14 Gd-based inorganic nanoagents attracted considerable attention^{15, 16}. Unfortunately, the hydration of
15 gadolinium-based nanoparticles suffers from high-temperature synthesis, though the consequent ion
16 leakage is minimized by the confined nanostructure compared with chelate complexes¹⁵.

17 Herein, we first introduce gadolinium ions into the ACC mineralization process, which have been
18 proven to be integrated into the final amorphous calcium carbonate phase. In this amorphous system,
19 gadolinium ions in conjunction with poly(acrylic acid) facilitated enhanced hydration water and stability
20 of nanoclusters, while the confinement of gadolinium ions by carbonate improved the biocompatibility
21 and performance, indicating the resulting product has noteworthy MRI contrast agent properties.
22 Furthermore, a mutual effect between the paramagnetic lanthanide gadolinium ion and amorphous

1 calcium carbonate is discovered, which contributes to the maximized hydrated content in the as-prepared
2 amorphous composite nanoclusters and an extremely high longitudinal relaxation. The final amorphous
3 nanoclusters possessed an extremely high water to Ca ratio (water/Ca = 7.2) compared with the normal
4 ACCs (ratios remained constant at about 0.4-1.9). The longitudinal relaxivity of ACNC (37.93 ± 0.63
5 $\text{mM}^{-1} \cdot \text{s}^{-1}$ under 3.0 T) has also benefited from the high water content, which is ten times higher than that
6 of the commercially available MR contrast agent gadopentetic acid (Gd-DTPA) and highly resistant to
7 ion leakage so it can serve as a potential MR contrast agent.

8 **Results**

9 **Characterization of ACNC.** So far, besides different kinds of organic additives such as biomolecules and
10 polymers, magnesium is the only inorganic cation that has been reported capable of stabilizing ACC^{6, 17}.
11 The gadolinium ion, whose ionic radius is closer to that of the calcium ion than that of the magnesium,
12 can be regarded as a smaller calcium ion analogue with higher valence and hydration energy^{18, 19}. Similarly
13 to the chelation between poly(acrylic acid) (PAA) and calcium for the enhanced stability of ACC^{7, 20},
14 carboxylate groups in PAA have the potential to chelate gadolinium ions, allowing the bound complex to
15 later be solidified into carbonate²¹.

16 As shown in Fig. 1A, calcium chloride and gadolinium chloride were first mixed with PAA, and
17 equimolar sodium carbonate solution was then added under robust stirring. This efficient synthesis at room
18 temperature proved to yield amorphous carbonate nanoclusters (ACNC) in the presence of both
19 gadolinium and PAA. Two liters of aqueous product can be facilely produced, indicating the scalability
20 and reproducibility of the method reported here (Fig. 1B). The presence of clusters dispersed in normal
21 saline was reflected by the Tyndall effect (Fig. 1C). As shown in Fig. 1D, the spherical morphology was
22 further investigated by cryo-TEM, and proved to be comparable with ACC as reported previously²². The

1 nanoclusters observed by STEM (fig. S1) were in accordance with HAADF-STEM observations and the
2 amorphous character of clusters was validated by SAED analysis (Fig. 1E). EDS data showed the uniform
3 distributions of gadolinium and calcium in the cluster aggregates (fig. S2, A and B).

4 ACNC exhibited no crystalline peak in the XRD pattern, even after being dispersed in aqueous solution
5 for 6 months (fig. S3). The ACNC was further studied by X-ray Absorption Spectroscopy (XAS) and
6 extended X-ray absorption fine structure (EXAFS) analysis, and the Ca-O short-range environment within
7 ACNC was revealed to closely relate to those in the ACC standard and previously reported ACCs^{10, 11, 23}
8 (Fig. 1, F and G, tables S1 and S2). The size distribution of ACNC received from SAXS fitting analysis
9 showed an average radius of 1.3 nm (Fig. 1, H and I). In addition, the particle size of ACNC was measured
10 by dynamic laser scattering to be approximately 7.46 ± 1.30 nm which is higher than the diameter from
11 SAXS of 2.6 nm due to intensity weighing (fig. S4).

12 Thermogravimetric analysis (TGA) and differential scanning calorimeter (DSC) results for ACNC
13 showed a loss over 20 wt% upon heating to 300 °C due to the dehydration of the ACC, indicating a high
14 water content of ACNC. In addition, the pyrolysis of PAA occurred between 300 and 500 °C, and carbonate
15 was decomposed above 550 °C (Fig. 1J and fig. S5). Based on the TGA result, the composition of ACNC
16 included approximately 20% water content, 40% PAA and 40% amorphous carbonate. The absorbance
17 observed in TGA coupled FTIR (TG-FTIR) on ACNC at 2358 and 2322 cm^{-1} above 550 °C corresponded
18 to the asymmetric stretching vibration of CO_2 from the decomposition of carbonate (Fig. 1K). As shown
19 in fig. S6, the split band at 1415 and 1454 cm^{-1} in Fourier transform infrared spectroscopy (FTIR) can be
20 assigned to the asymmetric stretch vibration of the carbonate ions in typical ACC environments¹⁹. A broad
21 peak centered at 1086 cm^{-1} attributed to the internal CO_3^{2-} symmetric stretch was further confirmed by
22 Raman spectroscopy (fig. S7).

1 **Highly hydrated content of ACNC.** In order to investigate the contribution of each component to the
2 highly hydrated content and ACC-like environment, a series of control samples with varying composition
3 were synthesized as listed in table S3, including a Gd-occluded ACC composite (ACC-Gd), PAA-
4 stabilized ACC (ACC-PAA), amorphous gadolinium carbonate (AGC), PAA-stabilized AGC (AGC-PAA)
5 and two carbonate-free chelates (PAA-Ca and PAA-Ca/Gd). XRD patterns and Raman spectra were
6 performed to identify the amorphous phase (fig. S8, A and B). In the absence of PAA, ACC-Gd showed a
7 typical morphology for aggregated ACC nanoparticles with a uniform distribution of Gd and Ca (fig. S9,
8 A to D). The extended X-ray absorption fine structure (EXAFS) results further confirmed the presence of
9 ACC-like environments (fig. S10, A and B).

10 Attractively, there was still a higher water content held in ACC-Gd as compared to pure ACC even in
11 deionized water for a long time. The weight loss before 300 °C of ACC-Gd and ACC powder exposed to
12 the air over 6 months was more than 10% and only 0.1%, respectively (fig. S11). In both TGA and
13 volumetric Karl Fischer titration measurement results, the weight loss before 300 °C could be assigned to
14 the loss of water, and ACNC exhibited the highest water content of calculative 20 wt.-% among the
15 products with different composition (Fig. 2A). According to previous reports, the water contents per mole
16 of calcium in additive-free ACC and PAA-stabilized ACC were typically located in the range of 0.4-1.58
17 and 1.33-1.93, respectively^{20, 24}. In contrary, both ACC-Gd and ACC-PAA showed a higher water to Ca
18 ratio, and the highest ratio was obtained in ACNC (water/Ca = 7.2) (Fig. 2B), indicating a synergetic
19 enhancement of water binding by PAA and Gd in these amorphous nanoparticles. More importantly, to
20 compare the ratio of water to Gd as listed in Fig. 2C, the hydrated content per mole gadolinium in the
21 presence of both ACC-like environment and PAA in ACNC is more than four times that of PAA-occluded
22 gadolinium carbonate (PAA-AGC). Compared with AGC, the presence of ACC in the Gd-ACC composite

1 also resulted in a two-fold increase of the hydrated content per gadolinium ion.

2 To investigate the origin of the hydration, analytical ultracentrifugation (AUC) was applied to determine
3 the hydration water of ACNC via the frictional ratio and Perrin function assuming a spherical shape seen
4 in the electron microscopy images (table S4). The samples show sedimentation coefficients in the order
5 of 10^{-13} s, which is typical for prenucleation clusters (PNCs) that have similar sizes²⁵. The ACNCs have a
6 diameter of 1.5 nm, which is even smaller than the one found by SAXS, though still in reasonable
7 agreement. Their molar mass of 2200 g/mol indicates that they consist of approximately 20 CaCO_3 ion
8 pairs including the Gd^{3+} ions. The determined amount of bound hydration water in solution of 8.8 mol
9 H_2O per CaCO_3 (and 23.0 mol H_2O per Gd^{3+}), is considerably higher than in common ACCs (Fig. 2, B
10 and C, table S5). Notably, the water content of ACNC determined by AUC is in reasonable agreement
11 with the results from TGA, considering that the hydration was determined in wet and dry states,
12 respectively⁶.

13 **Stable high relaxivity of ACNC.** Besides the contribution of the dopant of the gadolinium ion to the
14 highly hydrated ACC content, a typical paramagnetic behavior was achieved in the amorphous carbonate
15 nanoclusters as shown in the M-H curve (Fig. 3A). Both the high hydration and confinement of the
16 gadolinium ions, the paramagnetic ACNC was conducive to increasing MRI contrast performance. The T_1
17 relaxation times of ACNC dispersed in normal saline at varying concentrations were measured using a 3.0
18 Tesla MR scanner. As shown in the T_1 map (Fig. 3B), the longitudinal relaxivity (r_1) of ACNC reached
19 $37.21 \text{ mM}^{-1}\cdot\text{s}^{-1}$ (Fig. 3C), which was ten times higher than that of commercially used Gd-DTPA ($3.19 \text{ mM}^{-1}\cdot\text{s}^{-1}$).
20 Besides the contribution from the large size of macromolecules and nanoparticles, ACNC possessed
21 four times higher longitudinal relaxivity compared to PAA modified amorphous gadolinium carbonate
22 (AGC-PAA) ($7.91 \text{ mM}^{-1}\cdot\text{s}^{-1}$), which was attributed to the high hydration content of ACC-like

1 environments. This high content of water may be primarily attributed to the stronger hydration ability of
2 trivalent Gd^{3+} as compared to divalent Ca^{2+} ions¹⁹, which reasonably enhanced inner-sphere and outer-
3 sphere relaxations of the ACC like environment occluded ACNC¹⁴. After three tests, the r_1 value of ACNC
4 was calculated to be approximately $37.93 \pm 0.63 \text{ mM}^{-1}\cdot\text{s}^{-1}$ (Fig. 3D).

5 In addition, r_1 and r_2 values of ACNC were measured under different magnetic fields (3.0 T and 0.5 T),
6 and its corresponding r_2/r_1 ratio was calculated (Fig. 3, E and F). The r_1 value of ACNC measured on 3.0
7 T was as high as $38.19 \text{ mM}^{-1}\text{s}^{-1}$, and the corresponding r_2 value and r_2/r_1 ratio were $72.49 \text{ mM}^{-1}\text{s}^{-1}$ and
8 1.90, respectively. Using a low field MR scanner system (0.5 T), the corresponding r_1 and r_2 values of
9 ACNC were $66.37 \text{ mM}^{-1}\text{s}^{-1}$ and $78.04 \text{ mM}^{-1}\text{s}^{-1}$, respectively, and the r_2/r_1 ratio was 1.18.

10 High stability is essential for gadolinium-based contrast agents, as transmetallation will lead to the
11 release of dissociated gadolinium ion with reported toxicity such as nephrogenic systemic fibrosis^{14, 26}.
12 Laurent and Muller reported the poor kinetic inertness against transmetallation for linear gadolinium-
13 based contrast agents such as commercially used Gd-DTPA²⁷. As shown in Fig. 3G, the PAA-Ca/Gd
14 chelate exhibited an even worse inertness than Gd-DTPA after exposure to Zn^{2+} in PBS for 48h. On the
15 contrary, ACNC demonstrably enhanced the stability against transmetallation, due to the gadolinium
16 confinement in ACC-like environments.

17 **Stability and biocompatibility of ACNC.** The absorption spectra of arsenazo III is generally used to detect
18 the leakage of gadolinium ion from Gd-based nanocomposite^{28, 29}. When the Arsenazo III aqueous solution
19 was mixed with Gd^{3+} , pink solution turned blue due to the formation of arsenazo- Gd^{3+} complex (Fig. 4A).
20 As shown in Fig. 4B, free gadolinium ion at a low concentration of $1 \mu\text{g/mL}$ was detectable by arsenazo
21 III mediated absorption spectra. However, in the normal saline dispersion of ACNC, no leakage of free
22 gadolinium ions in one week dialysis was detected using this colorimetric analysis, which was further

1 confirmed by ICP-MS (Fig. 4C). In sharp contrast to ACNC, PAA-Ca/Gd chelate showed an obvious
2 leakage compared with ACNC, further confirming the confinement of gadolinium ions by carbonate.

3 Moreover, ACNC was dispersed in human serum at 1 mmol (Gd) /L. Meanwhile, to simulate the
4 elevated phosphate concentrations in serum in patients with end-stage renal disease³⁰, the same
5 concentration of ACNC was dispersed in human serum supplemented an additional phosphate
6 concentration of 10 mmol/L for 15 days, followed by dialysis at different time points. No leakage of free
7 gadolinium ions was detected in dialysates using ICP-MS and colorimetric analysis (Fig. 4, D and E, fig.
8 S12), indicating the low dissociation risk for ACNC in the retention period *in vivo*.

9 To determine whether ACNC cause hemolysis, ACNC at different concentrations were incubated with
10 human blood serum at 37 °C for a hemolysis test. According to the standard, ACNC have no
11 haemocytolysis even at a high concentration of 0.5 mg (Gd) /mL, suggesting a good blood compatibility
12 (Fig. 4F). MTT assay was used as an evaluation of cytotoxicity by co-culturing human umbilical vein
13 endothelial cells (HUVEC) with ACNC for 24 h. No obvious reduction of viability in cells was induced
14 after exposure to ACNC, even at a high concentration of 0.5 mg (Gd) /mL (fig. S13). Encouraged by the
15 results thus far, a series of subcellular compatibility studies were carried out using human renal tubular
16 epithelial cell (HK-2). Healthy mitochondria of HK-2 cells were demonstrated by mitochondrial
17 membrane potentials (MMP) study (fig. S14). The immunofluorescent TdT-mediated dUTP Nick-End
18 Labeling (TUNEL) staining assay of HK-2 showed ACNC had no accumulated damage to the nuclear
19 DNA of cells (fig. S15). An EdU (5-Ethynyl-2'-deoxyuridine) assay was performed and confirmed that
20 ACNC had no effects on cell proliferation (fig. S16).

21 Meanwhile, histological sections of kidney and other major organs were collected 2 weeks after the
22 intravenous injection in mouse at a dose of 5 mg Gd/kg, and no evidence of pathologic change was

1 identified in H&E stained images (fig. S17, and fig. S18). 3 days and 3 weeks after intravenous injection
2 of ACNC in mouse, all hematologic and biochemical parameter values were in accordance with the
3 standard range and our control groups (fig. S19). To further test in the large animal beagle dog at a high
4 dosage (9 mg Gd/kg bw), there was no obvious difference of hematologic and biochemical parameters
5 between control and experimental groups after intravenous injection (fig. S20), suggesting that
6 physiological functions were not impaired by ACNC.

7 ***In vivo* MR imaging and metabolism of ACNC.** The enhancement of T_1 weighted MRI performance of
8 ACNC was further confirmed by MR angiography in rat, rabbit and beagle dog. After the bolus
9 intravenous injection of ACNC at a low dose (3 mg/kg bodyweight), jugular, carotid, aorta and caudal
10 vena cava can be clearly identified (Fig. 5, A to C), and the dosage is less than 1/5 of the typically
11 employed value in clinic. The whole-body angiography images of rat, rabbit and upper body of beagle dog
12 exhibited better angiographic contrast and more details in comparison with that of the Gd-DTPA control
13 group. As shown in Fig. 5D, the contrast enhancement of ACNC *in vivo* was further quantitatively
14 reflected by the mean value of signal-noise ratio (SNR) on rabbit and beagle dog, respectively³¹.

15 Recently, clinical translation of nanosized biomaterials attracted great attention, promising the
16 development of novel and specific nanomedical tools for diagnosis and therapy^{16, 32-35}. To avoid the
17 potential risk *in vivo*, renal clearance is the desirable and preferred excretion route for medical agents for
18 minimal catabolism and body exposure. However, compared to small molecular contrast agents, nanosized
19 MR contrast agents, especially the FDA approved nanosized iron oxide injections suffer from their poor
20 renal excretion as a result of their large size distribution (>20 nm)³⁶. Besides the conventional elimination
21 from liver (fig. S21), the quick renal clearance of ACNC from blood vessels was observed in the MRA
22 images after intravenous injection (fig. S22, A and B). Moreover, the bladder of beagle dog was also

1 brightened within 20 minutes in the T_{1w} image (fig. S23). In addition, as shown in the blood concentration-
2 time curve in mouse and beagle dog measured by ICP-AES, it could be effectively cleared from blood
3 vessels in 6 hours and there is rarely any residual content of gadolinium after 24 h (Fig. 6, A and B). In
4 the collected rat urine after the intravenous injection of ACNC, the content of gadolinium was detected by
5 ICP-AES and demonstrated a renal clearance efficiency of approximately 13% ID at 24 h (fig. S24), which
6 is comparable to that of gold nanoclusters with similar diameters³⁷. Abundant SAED amorphous cluster
7 aggregates could be observed in TEM images of dialyzed urine (Fig. 6C), and EDS mapping revealed a
8 matching distribution of gadolinium, calcium, carbon and oxide elements in these aggregates
9 corresponding to ACNC (Fig. 6, D and E). Physicochemical and physiological stability in synergy with
10 low injection dosage and partial clearance via kidney led to *in vivo* biocompatibility and potential
11 translational ability of these gadolinium-based amorphous carbonate clusters.

12 Discussion

13 A number of gadolinium-based contrast agents have been designed and approved worldwide for T_1 MR
14 imaging¹⁴. As a result of a high density of free electrons in the valence band and versatile functionalization
15 to interact with biomolecules *in vivo*, inorganic nanomaterials serving as contrast agents in various
16 imaging modalities are anticipated to achieve the clinical translation of nanomedicine^{15,38}. Therefore, the
17 scientists studied indefatigably including diverse fabrication methods and clearing pharmacokinetics in
18 order to investigate the translatability of Gd-based inorganic nanoparticles¹⁶. In consideration of the hazard
19 originated from the release of free Gd ions, a specific aim was to reduce the dose of injected nanoparticles
20 via the enhanced performance.

21 The hydration level plays a significant role in determining the contrasting performance of a MR contrast
22 agent¹⁴. Unfortunately, the hydration content of Gd-based nanocrystals is limited by traditional high

1 temperature synthesis processes¹⁵. Worth mentioning is that the high moisture content, including interior
2 water and deeply located structural water is the most distinctive feature of ACC⁷⁻¹¹. However, the potential
3 application of unstable hydrated ACC is largely ignored. Interestingly, the ionic radius of the gadolinium
4 ion is very close to that of the calcium ion, implying a possible interaction between gadolinium ions and
5 calcium ions that can be exploited by us.

6 In summary, our study confirms mutual effects between the paramagnetic lanthanide gadolinium ion
7 and amorphous calcium carbonate, which is beneficial to maximizing the water content in the obtained
8 amorphous composite nanoclusters. The material is synthesized through a facile one-pot process at room
9 temperature, enabling the large scale and cost effective production. Importantly, this high water content
10 contributes to the transparent MRI contrasting enhancement of gadolinium-based nanoclusters. In
11 combination with their low toxicity, partial renal clearance and easy potential for mass production, our
12 work enables further identification of the biomedical potential of ACC composites, and we anticipate that
13 it could lead to a new generation of more efficient diagnostic agents on the basis of amorphous
14 nanoclusters in the future.

1 **Methods**

2 **Materials.** Anhydrous calcium chloride, anhydrous sodium carbonate and ethyl alcohol were purchased
3 from Sinopharm Chemical Reagent Co. Ltd (Shanghai). Gadolinium chloride hexahydrate ($\text{GdCl}_3 \cdot 6\text{H}_2\text{O}$,
4 99.95%) were purchased from Yutai QingDa Fine Chemical Co., Ltd. (Shandong, China). Poly(acrylic
5 acid) (PAA, $M_w \approx 1800$) was purchased from Aldrich. All reagents were used as received without further
6 purification. The commercially used Gd-DTPA was produced by Guangdong Consun Pharmaceutical
7 Group, China (specification: 20 mL).

8 **Sample preparation.** In a typical procedure to synthesize additive-free amorphous calcium carbonate
9 (ACC), 10 mL Na_2CO_3 aqueous solution ($0.1 \text{ mol} \cdot \text{L}^{-1}$, 10 mL) was poured into calcium chloride (0.1
10 $\text{mol} \cdot \text{L}^{-1}$, 10 mL) aqueous solutions under vigorous magnetic stirring for 15 seconds. The aqueous
11 suspension after adding 20 mL ethanol were centrifuged at 3000 rpm for 2 min immediately, then the
12 precipitates were washed by ethanol, centrifuged for 5 min at 8000 rpm twice.

13 In a typical procedure to synthesize ACNC, anhydrous calcium chloride (CaCl_2 , $0.1 \text{ mol} \cdot \text{L}^{-1}$),
14 gadolinium chloride hexahydrate (GdCl_3 , $0.02 \text{ mol} \cdot \text{L}^{-1}$) and PAA (0.45 g) were dissolved in 10 mL DIW
15 with magnetic stirring. Anhydrous sodium carbonate (Na_2CO_3 , $0.1 \text{ mol} \cdot \text{L}^{-1}$, 10 mL) was poured into the
16 above solution with vigorous magnetic stirring for 1 min. 20 mL of ethanol was added to terminate the
17 reaction. The mixture was immediately centrifuged for 2 min at 3000 rpm, and precipitates were re-
18 suspended by DIW, centrifuged for 5 min at 8000 rpm twice. For liter-scale synthesis, the reaction volume
19 was scaled up 50 times and proceeded under robust mechanical agitation.

20 For the synthesis of ACC stabilized by PAA (ACC-PAA), 0.45 g PAA was used in the synthesis process
21 without the addition of gadolinium salt, and the product was washed by ethanol. For the preparation of

1 ACC-Gd, PAA was absent in the synthesis process and anhydrous CaCl_2 ($0.1 \text{ mol}\cdot\text{L}^{-1}$) and GdCl_3 (0.02
2 $\text{mol}\cdot\text{L}^{-1}$) were mixed in 10 mL DIW. Then the obtained ACC-Gd was washed by ethanol.

3 In a typical procedure to synthesize amorphous gadolinium carbonate (AGC) and AGC-PAA, Na_2CO_3
4 ($0.1 \text{ mol}\cdot\text{L}^{-1}$, 10 mL) was poured into 10 mL GdCl_3 aqueous solution ($0.067 \text{ mol}\cdot\text{L}^{-1}$, $\text{mol}[\text{GdCl}_3]:$
5 $\text{mol}[\text{Na}_2\text{CO}_3] = 2: 3$) under vigorous magnetic stirring for 15 seconds, then 20 mL ethanol was poured
6 into the aqueous suspension. After centrifuged at 3000 rpm for 2 min immediately, the precipitates were
7 washed by ethanol, centrifuged for 5 min at 8000 rpm twice. In addition, in the presence of 0.45 g PAA
8 in the GdCl_3 aqueous solution, AGC-PAA was prepared in the same procedure.

9 **Characterization.** Transmission electron microscopy (TEM) were carried out on H7700 (Hitachi, Japan)
10 with an acceleration voltage of 100 KV. Cryotransmission electron microscopy (cryo-TEM) was
11 performed on Tecnai F20 Transmission Cryo-Electron Microscopy. High-angle annular dark field
12 scanning TEM (HAADF-STEM), energy dispersive spectrometer (EDS) and EDS mapping were
13 performed on a field emission high resolution transmission electron microscope (FEI, Talos F200X). The
14 hydrodynamic diameter was calculated on a Nano ZS-90 Zetasizer (Malvern Instruments Corp, UK). X-
15 ray powder diffraction (XRD) patterns were performed on a rotating anode X-ray diffractometer
16 (SmartLabTM 9kW). FT-IR spectra were recorded with a Thermo Nicolet 8700 FT-IR spectrometer at room
17 temperature. Raman spectra were recorded using a Horiba LabRAM high-resolution (HR) Evolution
18 Raman spectrometer. The light source of the microscope was transferred to a diode laser (780 nm). The
19 spectra were scanned for $3 \times 100 \text{ s}^{39, 40}$. Thermogravimetric analysis (TGA), differential scanning
20 calorimeter (DSC) and thermogravimetry analysis coupled with Fourier transform infrared spectroscopy
21 (TG-FTIR) were recorded at a heating rate of 10 K min^{-1} under nitrogen flow on a TGA thermal analyzer
22 (NETZSCH STA 449F3). Magnetic investigation was carried on a superconducting quantum interface

1 device (SQUID) magnetometer (Quantum Design SQUID-VSM). ICP-AES were performed on an Optima
2 7300 DV instrument. UV-vis spectra were measured on a Shimadzu UV-2600 spectrophotometer at room
3 temperature.

4 **Small-angle X-ray scattering (SAXS).** Small-angle X-ray scattering (SAXS) analysis were
5 performed on a SAXSpoint 2.0 (Anton Paar). The size distribution function as determined by SAXS is
6 evaluated using GIFT (Generalized indirect Fourier transformation) software with precondition of
7 homogeneous spheres weighted by number. It is calculated using the following formulas⁴¹:

$$8 \quad I(q) = \int_0^{R_{max}} R^6 \cdot D_N(R) \cdot \left(3 \cdot \frac{\sin(qR) - qR\cos(qR)}{(qR)^3} \right)^2 \cdot dr$$

9 **EXAFS sample preparation, measurement and data fitting.** X-ray Absorption Spectroscopy
10 (XAS) measurements at the calcium K-edge (4.0381 keV) were undertaken at the Elettra synchrotron
11 Italy, operating at an energy of 2 GeV and current of 300 mA. Samples were ground in an agate mortar,
12 diluted with graphene powder and compacted into thin pellets. An optimal sample thickness of ~300 μm
13 and optimal calcium concentration after optimal dilution with graphene powder was prepared for each
14 sample including ACNC, ACC-Gd and ACC standards. Three full scans per sample of the X-ray
15 absorption near edge structure (XANES) and extended X-ray absorption fine structure (EXAFS) were
16 collected in transmission mode using a FMB-OXFORD ion chamber detector, in steps of 5 eV in the
17 pre-edge region (from 3738.43 eV to 4028.53 eV) and 0.2 eV in the edge region (from 4061.51 eV to
18 4061.71 eV), gradually increasing to 2.6 eV in the post-edge region (4061.71 eV to 4589.30 eV) up to k
19 = 13. Alignment, energy calibration and deglitching were performed using built-in features of the
20 Athena software package⁴². The first coordination shell around calcium (Ca-O) was fitted by generating
21 a single scattering pathway of Ca-O based on crystallographic data of calcite. Analysis of single
22 scattering pathways was undertaken from 1.3 to 2.53 Å in R space on Fourier transformed k²-weighted

1 data from 3 to 9.1 Å. Standards errors associated with the EXAFS data fitting over the k-range used here
2 are 15% for the first-shell coordination number, 0.03 Å for the radial distance and 15% for the Debye-
3 Waller factors.

4 Independent data points were determined by Stern's rule defining the fundamental limitation to the
5 amount of information that can be determined by XAFS. According to Stern's rule, the number of
6 parameters (N_{par}) used for the fit should be strictly inferior to the number of independent (N_{ind}) parameters
7 defined as $2\Delta k\Delta R/\pi + 2$, where Δk and ΔR are the fitted range in k and R space, respectively^{43, 44}. If $N_{\text{ind}} <$
8 N_{par} , the model cannot be taken as a proof of the coordination environment because the data set is
9 underdetermined by the level of complexity of the model. In this case, $N_{\text{ind}} = 7.5$ for ACC standard, ACC-
10 Gd and ACNC sample, $N_{\text{ind}} = 8.16$ for ACC-PAA and $N_{\text{par}} = 4$ as such that $N_{\text{ind}} > N_{\text{par}}$. The multi-
11 component model yielding the best fit of the experimental data is considered as reasonable and can thus
12 be considered as a likely representation to characterize the calcium coordination environment. Linear
13 combination was performed on the XANES and near-EXAFS region (from 30 Å⁻¹ before to 80 Å⁻¹ after
14 edge jump). Samples ACC-Gd, ACNC and PAA-Gd/Ca were compared to standards samples ACC-PAA
15 and PAA-Ca.

16 **Analytical ultracentrifugation (AUC).** The AUC measurements were performed on a modified Optima
17 XL-A (Beckman Coulter, Palo Alto, CA, United States) using an absorbance optics and an advanced
18 Rayleigh interference optics developed by Nanolytics⁴⁵. 12-mm path length double-sector titanium
19 centerpieces with sapphire windows (Nanolytics, Potsdam, Germany) were used for all experiments. For
20 ACNC sample measurement, the original ACNC sample was pre-sedimented on a UNIVERSAL 320
21 Hettich centrifuge (Hettich, Tuttlingen, Germany) for 20 min at 9 000 rpm. 360 µL of pretreated ACNC
22 solution was used in the sample sector and 360 µL of a 1:175 diluted (with 0.154 M NaCl) pre-reaction

1 PAA-Ca/Gd solution (aqueous mixture including PAA, calcium chloride and gadolinium chloride) in the
2 reference sector. For PAA sample measurement as reference, 10 mg PAA (1800 Da) were dissolved in 1
3 mL of 0.154 M NaCl solution. All samples were investigated at 20 °C and 60 000 rpm, corresponding to
4 a centrifugal force up to 290 000 g.

5 Sedimentation velocity data were evaluated with Sedfit and UltraScanIII. In Sedfit (version 16.1c by
6 Peter Schuck⁴⁶), the ls-g*(s) and continuous c(s,ff₀) models were used. For calculation of the
7 sedimentation coefficient distributions g(s) with the least-squares-g*(s) model⁴⁷, data were fitted with a
8 Tikhonov-Phillips regularization using a confidence level (F-ratio) of 0.683 and a resolution of 100 grid
9 points. For determination of the sedimenting particle density⁴⁸ with the c(s,ff₀) analysis⁴⁹, data were fitted
10 with a maximum entropy regularization using a confidence level (F-ratio) of 0.683 and a resolution of 100
11 grid points in s and 10-20 grid points in f/f₀. The 2D c(s,ff₀) distributions were plotted using MATLAB
12 software version R2017b, 64 bit from MathWorks. For calculation of the sample density from 2D
13 distributions, a MATLAB mask script developed by Quy Khac Ong⁵⁰ was used. For characterization of
14 anisotropy, UltraScanIII⁵¹ (version 4.0, revision 5699) was used for performing the two-dimensional
15 spectrum analysis (2DSA)⁵². The 2DSA-Monte Carlo (MC) analyses were performed with 50 iterations
16 on a supercomputer.

17 The function defining the shape, flexibility and degree of solvation (by water, salt ions, and any other
18 solvent molecules) of the macromolecule is the *Perrin translational frictional function*, P (see following
19 equation). This degree of water association is termed the hydration of the solute, δ , and is defined as the
20 mass in grams of associated solvent per gram of anhydrous solute⁵³.

$$21 \quad P = \frac{f}{f_0} \left(\frac{\bar{v}}{\bar{v}_s} \right)^{1/3} = \frac{f}{f_0} \left(\frac{\bar{v}}{\bar{v} + \delta \bar{v}_{H_2O}} \right)^{1/3}$$

22 where f/f_0 is the frictional ratio (which is the dimensionless ratio of the observed translational

1 frictional coefficient f to that of an equivalent spherical molecule of the same anhydrous mass and density
2 f_0 , \bar{v} is the partial specific volume (cm^3/g) of the solute and \bar{v}_s is the hydrated specific volume (the
3 volume occupied by the solute and associated solvent per unit mass of the anhydrous solute) and $\bar{v}_{H_2O} =$
4 specific volume of water given as:

$$5 \quad \bar{v}_s = \bar{v} + \delta \bar{v}_{H_2O}$$

6 If all excess friction is due to the hydration and the solute is a sphere, then P is 1^{54} and the hydration
7 can be calculated as:

$$8 \quad \delta = \frac{\left[\left(\frac{f}{f_0}\right)^3 - 1\right] \bar{v}}{\bar{v}_{H_2O}} = \left[\left(\frac{f}{f_0}\right)^3 - 1\right] \bar{v} \rho_{H_2O}$$

9 **Hydrated content analysis.** The moles of water molecules per mole of CaCO_3 was thus calculated
10 according to the result of inductively coupled plasma atomic emission spectroscopy (ICP-AES), TG
11 analysis and volumetric Karl Fischer titration measurement. Titration measurement was performed on a
12 Karl Fischer moisture titrator (V10S, volumetric KF titrator, Mettler Toledo). The hydrated content was
13 assigned to be the weight loss starting from the endothermic peak to 300°C , while the content of Ca^{2+} and
14 Gd^{3+} ions were determined by ICP-AES. The molar ratio between water and Ca^{2+} ions in ACC can thus
15 be calculated according to previous reports^{20, 55, 56}.

16 **Leakage studies of Gd^{3+} ion.** The detection of leakage of gadolinium ion was carried out using a method
17 reported previously^{28, 29, 57}. ACNC were dispersed in a series of simulative physiological environment
18 including normal saline, human serum and human serum supplemented an additional phosphate
19 concentration of 10 mmol/L . ACNC was dispersed with a final concentration of 1 mmol (Gd) /L . The
20 dialysis of ACNC was performed at 37°C for 7 days using a dialysis bag (MWCO 1000 Da). The
21 concentration of gadolinium in dialysates collected at different time points was measured by both

1 Arsenazo III mediated chromogenic assay and ICP-AES. In the chromogenic assay, the collected
2 dialysates were mixed with Arsenazo III (0.05 mM) dissolved in chloroacetic acid-sodium hydroxide
3 buffer solution (pH 2.8), and the absorption at 658 nm was detected. Normal saline and GdCl₃ solution
4 were used as negative and positive controls, respectively.

5 ***In vitro* biocompatibility studies.** Human umbilical vein endothelial cells (HUVEC) were cultured in
6 Dulbecco's modified Eagle's medium. Cell viability was performed by standard MTT method. Briefly,
7 cells were plated at the density of about 1x10⁴ cells per well in 96-well plate, and incubated for 12 h. Then
8 DMEM culture medium with ACNC were added, and cells were exposed to ACNC at various
9 concentrations for 24 h. Then 10 μL of MTT solution (5 mg/mL in PBS) was added to each well for
10 additional 4 h incubation at 37 °C. After removing the medium, 150 μL of DMSO was added to dissolve
11 the formed formazan crystals in each well, and the optical density of the solution was measured at 570 nm
12 using Microplate Reader (BioTek Instruments, USA). Human renal tubular epithelial (HK-2) cells were
13 used for mitochondrial membrane potentials (MMP) assay, TdT-mediated dUTP Nick-End Labeling
14 (TUNEL) assay and 5-Ethynyl-2'-deoxyuridine (EdU) assay. Mitochondrial membrane potential assay kit
15 with J-aggregates (JC-1) (Beyotime, Shanghai, China), one step TUNEL apoptosis assay kit (Beyotime,
16 Shanghai, China), and EdU cell proliferation kit with Alexa Fluor 555 (Beyotime, Shanghai, China) were
17 employed.

18 **Animal studies.** Specific pathogen Free (SPF) BALB/c mice (male, 6 weeks), New Zealand rabbit (male,
19 2 kg) and Beagle dog (male, 6 kg) were purchased from Anhui Medical University. Animal studies were
20 performed in accordance with the recommendations in the Guide for the Care and Use of Laboratory
21 Animals of the National Institutes of Health. The *in vivo* compatibility studies and *in vivo* MRI studies
22 were under protocols approved by the Institutional Animal Care and Use Committee (IACUC) of Anhui

1 Medical University (LLSC20150134).

2 ***In vivo* biocompatibility studies.** ACNC normal saline solutions were intravenously injected in mice (via
3 tail vein) at a dosage of 5 mg Gd/kg bodyweight and Beagle dog (via hindlimb vein) at a dosage of 9 mg
4 Gd/kg bodyweight. For evaluation of blood index and biochemical index, mice were sacrificed by
5 anesthetics for 3 days and 3 weeks after intravenous injection, respectively. Blood of Beagle dogs were
6 collected every two weeks via hindlimb vein. Blood samples were collected by the anticoagulant blood
7 collection tubes and separating gel tubes. The examination of blood index and biochemical index were
8 carried out on Sysmex XE2100 and Vitros 5600, respectively.

9 ***In vivo* metabolic study.** ACNC normal saline solutions were intravenously injected into twenty mice
10 (male, 20 g) at 3 mg Gd/kg bodyweight (0.5mg Gd/mL, 120 μ L) via rapid manual injection for
11 a simulated bolus injection study. These mice were randomly divided into four groups, and various organs
12 were resected from the mice in each group 1, 7, 15 and 30 days after intravenous injection, respectively.
13 The urine samples were collected at 12 hours after *i.v.* injection of ACNC on rat at 5 mg Gd/kg bodyweight,
14 followed by dialysis at 25 °C. After 24 hours, the dialysates in dialysis bags (MWCO=1000 Da) were
15 collected for further characterization.

16 **MRI acquisition and analysis.** ACNC and Gd-DTPA dispersed in normal saline at gradient
17 concentrations in 5 mL microtubes were placed on a support immersed in NiSO₄ solution. The
18 concentrations of gadolinium were measured by ICP-AES. MR T_1 map were acquired using an inversion
19 recovery sequence on a 3.0 Tesla MR scanner (Trio Tim, Siemens) equipped with a head coil. Imaging
20 parameters were as follows: repetition time (TR) = 4000 ms, echo time (TE) = 14 ms, inversion time (TI)
21 from 25 to 3500 ms (TI included 25, 50, 75, 100, 150, 200, 250, 300, 350, 400, 500, 600, 800, 1000, 1500,
22 2000, 2500, 3000, 3500 ms), field of vision (FOV) = 220×144 mm². The longitudinal relaxivity (r_1) was

1 calculated as follow according to an equation reported previously with a concentration gradient from 0.025
2 to 0.4 mM of gadolinium ion. The inverse of the relaxation time ($1/T_1$, s^{-1}) was plotted against the
3 concentration of gadolinium, and the slope of the plot was the relaxivity of the agent ($mM^{-1}\cdot s^{-1}$)^{58, 59}. The
4 measurements on a low field MR scanner system were performed using a 0.5T LF-NMR instrument at
5 32 °C provided by Suzhou Niumag Analytical Instrument Corporation.

6 ***In vivo* MR angiography analysis.** After complete intravenous anaesthesia, animals were fixed onto
7 different supports with suitable size. Then, ACNC dispersed in normal saline or Gd-DTPA diluted by
8 normal saline were injected intravenously. Rat was injected from caudal vein using an indwelling needle
9 at a dose of 2.5 mg Gd/kg. Bolus injection on rabbit and beagle dog were performed at a dose of 3 mg
10 Gd/kg from forelimb veins by mechanical high-pressure injector (Optistar LE, Mallinckrodt, USA).
11 FLASH 3D sequence was employed to collect angiographic data. The detailed parameters of MR
12 angiography of rat were as follows: A knee coil was used. TR = 3.95 ms, TE = 1.9 ms, FOV: 210×280
13 mm². The time of acquisition (TA) was 24.62 seconds. Flip angle (FA) was 20. Acquisition matrix was
14 288p * 512. Acquisition number and number of averages were both 1. The detailed parameters of MR
15 angiography of rabbit were as follows: A local head and neck coil were used. TR = 3.6 ms, TE = 1.65 ms,
16 FOV: 210×280 mm². The time of acquisition (TA) was 23.4 seconds. Flip angle (FA) was 18. Acquisition
17 matrix was 288p * 512. Acquisition number and number of averages were both 1. The detailed parameters
18 of MR angiography of beagle dog were as follows: A local head and neck coil, spine coil, and
19 radiofrequency body transmit coil were used. TR = 3.19 ms, TE = 1.28 ms, FOV: 240×320 mm². The time
20 of acquisition (TA) was 20.74 seconds. Flip angle (FA) was 16. Acquisition matrix was 288p * 512.
21 Acquisition number and number of averages were both 1. The images were processed firstly by Siemens
22 Syngo MR workstation.

1 Signal-noise ratio (SNR) was calculated in a single image (κ) based on two separate regions of interest
 2 (ROIs). One in the vessel of interest (ROI_{vessel}) were measured by placing a signal at the same ROI in the
 3 same slice both in Gd-DTPA and ACNC group, which was recorded as the mean signal intensities of vessel
 4 (S_{vessel}). One in the image background ($ROI_{background}$) was located in an artifact-free homogeneous area,
 5 which was defined as the background signal ($S_{background}$)³¹. SNR corresponds to the ratio between S_{vessel}
 6 and $S_{background}$ as follow:

$$7 \quad SNR_{stdv}(\kappa) = \frac{S_{vessel}}{S_{background}} = \frac{\frac{\text{mean}_{r \in ROI_{vessel}}(S_N(r, \kappa))}{\sqrt{\frac{2}{4 - \pi}}}}{\frac{\text{stddev}_{r \in ROI_{background}}(S_N(r, \kappa))}{\sqrt{\frac{2}{4 - \pi}}}} = \frac{m_{vessel}}{\sqrt{\frac{2}{4 - \pi}} S_{background}}$$

8 Three ROIs were selected in descending aorta, aortic arch and ascending aorta on rabbit, and four
 9 regions in brachiocephalic trunk artery, left subclavian artery, left common carotid artery and right branch
 10 of olfactory artery were measured on beagle dog, respectively.

11 **Statistical analysis.** All data were expressed as mean \pm S.E.M. and analyzed by independent samples t-
 12 tests. A value of $P < 0.05$ was considered statistically difference. (* $P < 0.05$, ** $P < 0.01$, *** $P < 0.001$).

13

14

15

16 **Data availability.** The data that support the findings of this study are available on request from the
 17 corresponding authors (Y.L., H.C. or S.-H.Y.).

18

19 References

- 20 1. De Yoreo, J. J., et al. Crystallization by particle attachment in synthetic, biogenic, and geologic
 21 environments. *Science* **349**, 10 (2015).
- 22 2. Politi, Y., Arad, T., Klein, E., Weiner, S., Addadi, L. Sea urchin spine calcite forms via a transient
 23 amorphous calcium carbonate phase. *Science* **306**, 1161-1164 (2004).
- 24

- 1
- 2 3. Xu, Y. F., et al. Microscopic structure of the polymer-induced liquid precursor for calcium
3 carbonate. *Nat. Commun.* **9**, 12 (2018).
- 4
- 5 4. Addadi, L., Raz, S., Weiner, S. Taking advantage of disorder: Amorphous calcium carbonate and
6 its roles in biomineralization. *Adv. Mater.* **15**, 959-970 (2003).
- 7
- 8 5. Liu, Z. M., et al. Crosslinking ionic oligomers as conformable precursors to calcium carbonate.
9 *Nature* **574**, 394-398 (2019).
- 10
- 11 6. Gower, L. B. Biomimetic model systems for investigating the amorphous precursor pathway and
12 its role in biomineralization. *Chem. Rev.* **108**, 4551-4627 (2008).
- 13
- 14 7. Du, H. C., Amstad, E. Water: How does it influence the CaCO₃ formation? *Angew. Chem. Int.*
15 *Edit.* **59**, 1798-1816 (2020).
- 16
- 17 8. Ihli, J., et al. Dehydration and crystallization of amorphous calcium carbonate in solution and in
18 air. *Nat. Commun.* **5**, 3169 (2014).
- 19
- 20 9. Alberic, M., et al. The crystallization of amorphous calcium carbonate is kinetically governed by
21 ion impurities and water. *Adv. Sci.* **5**, 9 (2018).
- 22
- 23 10. Farhadi-Khouzani, M., Chevrier, D. M., Zhang, P., Hedin, N., Gebauer, D. Water as the key to
24 proto-aragonite amorphous CaCO₃. *Angew. Chem. Int. Edit.* **55**, 8117-8120 (2016).
- 25
- 26 11. Gebauer, D., et al. Proto-calcite and proto-vaterite in amorphous calcium carbonates. *Angew.*
27 *Chem. Int. Edit.* **49**, 8889-8891 (2010).
- 28
- 29 12. Zou, Z. Y., et al. A hydrated crystalline calcium carbonate phase: Calcium carbonate
30 hemihydrate. *Science* **363**, 396-400 (2019).
- 31
- 32 13. Smeets, P. J., Cho, K. R., Kempen, R. G., Sommerdijk, N. A., De Yoreo, J. J. Calcium carbonate
33 nucleation driven by ion binding in a biomimetic matrix revealed by in situ electron microscopy.
34 *Nat. Mater.* **14**, 394-399 (2015).
- 35
- 36 14. Wahsner, J., Gale, E. M., Rodriguez-Rodriguez, A., Caravan, P. Chemistry of MRI contrast
37 agents: current challenges and new frontiers. *Chem. Rev.* **119**, 957-1057 (2019).
- 38
- 39 15. Dong, H., et al. Lanthanide nanoparticles: from design toward bioimaging and therapy. *Chem.*
40 *Rev.* **115**, 10725-10815 (2015).
- 41
- 42 16. Huang, H., Feng, W., Chen, Y., Shi, J. L. Inorganic nanoparticles in clinical trials and
43 translations. *Nano Today* **35**, 100972 (2020).
- 44
- 45 17. Loste, E., Wilson, R. M., Seshadri, R., Meldrum, F. C. The role of magnesium in stabilising

- 1 amorphous calcium carbonate and controlling calcite morphologies. *J. Cryst. Growth* **254**, 206-
2 218 (2003).
- 3
- 4 18. Shannon, R. D. Revised effective ionic radii and systematic studies of interatomic distances in
5 halides and chalcogenides. *Acta Crystallogr. A* **A32**, 751-767 (1976).
- 6
- 7 19. Smith, D. W. Ionic hydration enthalpies. *J. Chem. Educ.* **54**, 540-542 (1977).
- 8
- 9 20. Huang, S.-C., Naka, K., Chujo, Y. A carbonate controlled-addition method for amorphous
10 calcium carbonate spheres stabilized by poly(acrylic acid)s. *Langmuir* **23**, 12086-12095 (2007).
- 11
- 12 21. Ünaleroğlu, C., Zümreoğlu-Karan, B., Özcan, S., Firat, T. Characterization and magnetic-
13 behavior of cobalt(II) and gadolinium(III) polyacrylates. *J. Appl. Polym. Sci.* **56**, 1239-1243
14 (1995).
- 15
- 16 22. Kellermeier, M., et al. Colloidal stabilization of calcium carbonate prenucleation clusters with
17 silica. *Adv. Funct. Mater.* **22**, 4301-4311 (2012).
- 18
- 19 23. Michel, F. M., et al. Structural characteristics of synthetic amorphous calcium carbonate. *Chem.*
20 *Mater.* **20**, 4720-4728 (2008).
- 21
- 22 24. Khouzani, M. F., et al. Disordered amorphous calcium carbonate from direct precipitation.
23 *Crystengcomm* **17**, 4842-4849 (2015).
- 24
- 25 25. Gebauer, D., Völkel, A., Cölfen, H. Stable prenucleation calcium carbonate clusters. *Science* **322**,
26 1819-1822 (2008).
- 27
- 28 26. Laurent, S., Elst, L. V., Copoix, F., Muller, R. N. Stability of MRI paramagnetic contrast media -
29 A proton relaxometric protocol for transmetallation assessment. *Invest. Radiol.* **36**, 115-122
30 (2001).
- 31
- 32 27. Laurent, S., Vander Elst, L., Henoumont, C., Muller, R. N. How to measure the transmetallation
33 of a gadolinium complex. *Contrast Media Mol. Imaging* **5**, 305-308 (2010).
- 34
- 35 28. Kumar, R., Nyk, M., Ohulchansky, T. Y., Flask, C. A., Prasad, P. N. Combined optical and MR
36 bioimaging using rare earth ion doped NaYF₄ nanocrystals. *Adv. Funct. Mater.* **19**, 853-859
37 (2009).
- 38
- 39 29. Wang, L. J., et al. A Gd-doped Mg-Al-LDH/Au nanocomposite for CT/MR bimodal imagings
40 and simultaneous drug delivery. *Biomaterials* **34**, 3390-3401 (2013).
- 41
- 42 30. Frenzel, T., Lengersfeld, P., Schirmer, H., Hutter, J., Weinmann, H. J. Stability of gadolinium-based
43 magnetic resonance imaging contrast agents in human serum at 37°C. *Invest. Radiol.* **43**, 817-828
44 (2008).
- 45

- 1 31. Dietrich, O., Raya, J. G., Reeder, S. B., Reiser, M. F., Schoenberg, S. O. Measurement of signal-
2 to-noise ratios in MR images: Influence of multichannel coils, parallel imaging, and
3 reconstruction filters. *J. Magn. Reson. Imaging* **26**, 375-385 (2007).
4
- 5 32. Park, S. M., Aalipour, A., Vermesh, O., Yu, J. H., Gambhir, S. S. Towards clinically translatable
6 in vivo nanodiagnostics. *Nat. Rev. Mater.* **2**, 19 (2017).
7
- 8 33. Lee, H., Shin, T. H., Cheon, J., Weissleder, R. Recent developments in magnetic diagnostic
9 systems. *Chem. Rev.* **115**, 10690-10724 (2015).
10
- 11 34. Chen, H. M., Zhang, W. Z., Zhu, G. Z., Xie, J., Chen, X. Y. Rethinking cancer nanotheranostics.
12 *Nat. Rev. Mater.* **2**, 18 (2017).
13
- 14 35. Min, Y. Z., Caster, J. M., Eblan, M. J., Wang, A. Z. Clinical translation of nanomedicine. *Chem.*
15 *Rev.* **115**, 11147-11190 (2015).
16
- 17 36. Du, B. J., Yu, M. X., Zheng, J. Transport and interactions of nanoparticles in the kidneys. *Nat.*
18 *Rev. Mater.* **3**, 358-374 (2018).
19
- 20 37. Du, B. J., et al. Glomerular barrier behaves as an atomically precise bandpass filter in a sub-
21 nanometre regime. *Nat. Nanotechnol.* **12**, 1096-1102 (2017).
22
- 23 38. Jin, Y. D., Jia, C. X., Huang, S. W., O'Donnell, M., Gao, X. H. Multifunctional nanoparticles as
24 coupled contrast agents. *Nat. Commun.* **1**, 8 (2010).
25
- 26 39. Raz, S., Hamilton, P. C., Wilt, F. H., Weiner, S., Addadi, L. The transient phase of amorphous
27 calcium carbonate in sea urchin larval spicules: The involvement of proteins and magnesium ions
28 in its formation and stabilization. *Adv. Funct. Mater.* **13**, 480-486 (2003).
29
- 30 40. Rodriguez-Navarro, C., Kudlacz, K., Cizer, O., Ruiz-Agudo, E. Formation of amorphous calcium
31 carbonate and its transformation into mesostructured calcite. *Crystengcomm* **17**, 58-72 (2015).
32
- 33 41. Glatter, O. Evaluation of small-angle scattering data from lamellar and cylindrical particles by
34 the indirect transformation method. *J. Appl. Crystallogr.* **13**, 577-584 (1980).
35
- 36 42. Ravel, B., Newville, M. ATHENA, ARTEMIS, HEPHAESTUS: data analysis for X-ray
37 absorption spectroscopy using IFEFFIT. *J. Synchrot. Radiat.* **12**, 537-541 (2005).
38
- 39 43. Stern, E. A. Number of relevant independent points in X-ray-absorption fine-structure spectra.
40 *Phys. Rev. B, Condens. Matter* **48**, 9825-9827 (1993).
41
- 42 44. Booth, C. H., Hu, Y. J. Confirmation of standard error analysis techniques applied to EXAFS
43 using simulations. In: DiCicco A, Filipponi A (eds). *14th International Conference on X-Ray*
44 *Absorption Fine Structure*, vol. 190. Iop Publishing Ltd: Bristol, 2009.
45

- 1 45. https://www.nanolytics-instruments.de/interference_optics_aida.
- 2
- 3 46. Schuck, P. P. S. v. c. <http://analyticalultracentrifugation.com/download.htm>.
- 4
- 5 47. Schuck, P., Rossmanith, P. Determination of the sedimentation coefficient distribution by least-
6 squares boundary modeling. *Biopolymers* **54**, 328-341 (2000).
- 7
- 8 48. Carney, R. P., et al. Determination of nanoparticle size distribution together with density or
9 molecular weight by 2D analytical ultracentrifugation. *Nat. Commun.* **2**, 335 (2011).
- 10
- 11 49. Brown, P. H., Schuck, P. Macromolecular size-and-shape distributions by sedimentation velocity
12 analytical ultracentrifugation. *Biophys. J.* **90**, 4651-4661 (2006).
- 13
- 14 50. Institute of Materials, École Polytechnique Fédérale de Lausanne (EPFL), Station 12, 1015
15 Lausanne, Switzerland E-mail: quy.ong@epfl.ch.
- 16
- 17 51. Demeler, B. U. v., release 2783. . A Comprehensive Data Analysis Software Package for
18 Analytical Ultracentrifugation Experiments. The University of Lethbridge, Department of
19 Chemistry and Biochemistry.
- 20
- 21 52. Brookes, E., Cao, W. M., Demeler, B. A two-dimensional spectrum analysis for sedimentation
22 velocity experiments of mixtures with heterogeneity in molecular weight and shape. *Eur.*
23 *Biophys. J. Biophys. Lett.* **39**, 405-414 (2010).
- 24
- 25 53. Harding, S. E. *Frictional coefficient, ratio*. In book: T. E. Creighton, . *Encyclopedia of Molecular*
26 *Biology*, (J. Wiley & Sons, New York, 1999). pp.1942.
- 27
- 28 54. C. R. Cantor, P. R. S. *Biophysical Chemistry. Part II. Techniques for the study of biological*
29 *structure and function*, (W. H. Freeman, 1980) pp. 1561-1586.
- 30
- 31 55. Ihli, J., Kulak, A. N., Meldrum, F. C. Freeze-drying yields stable and pure amorphous calcium
32 carbonate (ACC). *Chem. Commun.* **49**, 3134-3136 (2013).
- 33
- 34 56. Radha, A. V., Forbes, T. Z., Killian, C. E., Gilbert, P., Navrotsky, A. Transformation and
35 crystallization energetics of synthetic and biogenic amorphous calcium carbonate. *Proc. Natl.*
36 *Acad. Sci. U. S. A.* **107**, 16438-16443 (2010).
- 37
- 38 57. Hvattum, E., Normann, P. T., Jamieson, G. C., Lai, J. J., Skotland, T. Detection and quantitation
39 of gadolinium chelates in human serum and urine by high-performance liquid chromatography
40 and post-column derivatization of gadolinium with Arsenazo III. *J. Pharmaceut. Biomed.* **13**,
41 927-932 (1995).
- 42
- 43 58. Fram, E. K., et al. Rapid calculation of T₁ using variable flip angle gradient refocused imaging.
44 *Magn. Reson. Imaging* **5**, 201-208 (1987).
- 45

- 1 59. Kim, B. H., et al. Large-scale synthesis of uniform and extremely small-sized iron oxide
2 nanoparticles for high-resolution T₁ magnetic resonance imaging contrast agents. *J. Am. Chem.*
3 *Soc.* **133**, 12624-12631 (2011).
4
5
6
7
8

1 **Acknowledgements**

2 This work was supported by the National Natural Science Foundation of China (Grants 51732011,
3 21431006, 21761132008, 51972090, 21501039, 51702309, 81801831), the Foundation for Innovative
4 Research Groups of the National Natural Science Foundation of China (Grant 21521001), Key Research
5 Program of Frontier Sciences, CAS (Grant QYZDJ-SSW-SLH036), the National Basic Research Program
6 of China (Grant 2014CB931800), the Users with Excellence and Scientific Research Grant of Hefei
7 Science Center of CAS (2015HSC-UE007), the Fundamental Research Funds for the Central Universities
8 (WK9110000062, JZ2018HGPA0269, WK2060190056), the China Postdoctoral Science Foundation
9 (2015M570540), the Natural Science Foundation of Anhui Province (1708085ME114), the
10 Major/Innovative Program of Development Foundation of Hefei Center for Physical Science and
11 Technology (2016FXZY005). The authors would like to thank Mei Sun, Yan-Wei Ding, Cheng-Min Wang,
12 Yu-Song Wang, Guan-Yin Gao, Yu-Feng Meng, Yong-Hong Song, Yang-Yi Liu in University of Science
13 and Technology of China, Hao Ding in Suzhou Niumag Analytical Instrument Corporation, He Chen, Li
14 Zhang and Hui Wang in The First Affiliated Hospital of Anhui Medical University, Duo An in Cornell
15 University, and Ye-Ping Li from Anton Paar China for useful assistance of this manuscript, and Luca Olivi,
16 Giuliana Aquilanti and Simone Pollastri in the XAFS beamline at Elettra Synchrotron for their help. D. G.
17 is a professor of the Leibniz Universität Hannover. J. A. is financed within the framework of the SFB 1214
18 (Collaborative Research Center funded by the German Research Foundation, DFG, project A02). H. C.
19 thanks the particle analysis center of the SFB 1214 for the AUC equipment.

20

21 **Author Contributions**

1 S.H.Y. and Y.L. conceived the idea, designed the experiments and supervised the research, L.D., C.S., Y.L.,
2 Y.Z., L.B.M., D.G., H.C., R.R., Y.D.W. and F.L. carried out the synthetic experiment and analysis. D.G.,
3 J.A., H.C. and L.D. worked on the EXAFS measurement and analysis. L.D., Y.Z., H.L.G., Z.P., H.Q.W.,
4 X.Y. and F.L. processed the biocompatible evaluation. L.D., Y.J.X., Y.D.W., Y.L., H.L.G., Z.P., X.Y., F.L.
5 and C.S. worked on the animal experiments, L.D., Y.J.X., Y.L., F.L. and C.S. investigated the MRI
6 performance, L.D., Y.J.X., C.S., D.G., Y.L., H.C. and S.H.Y. wrote the paper, all authors discussed the
7 results and commented on the manuscript.

8

9 **Additional information**

10 **Supplementary Information** accompanies this paper at <http://www.nature.com/naturecommunications>

11 **Competing interests:** The authors declare no competing interests.

12 **Reprints and permissions** information is available online at
13 <http://npg.nature.com/reprintsandpermissions/>

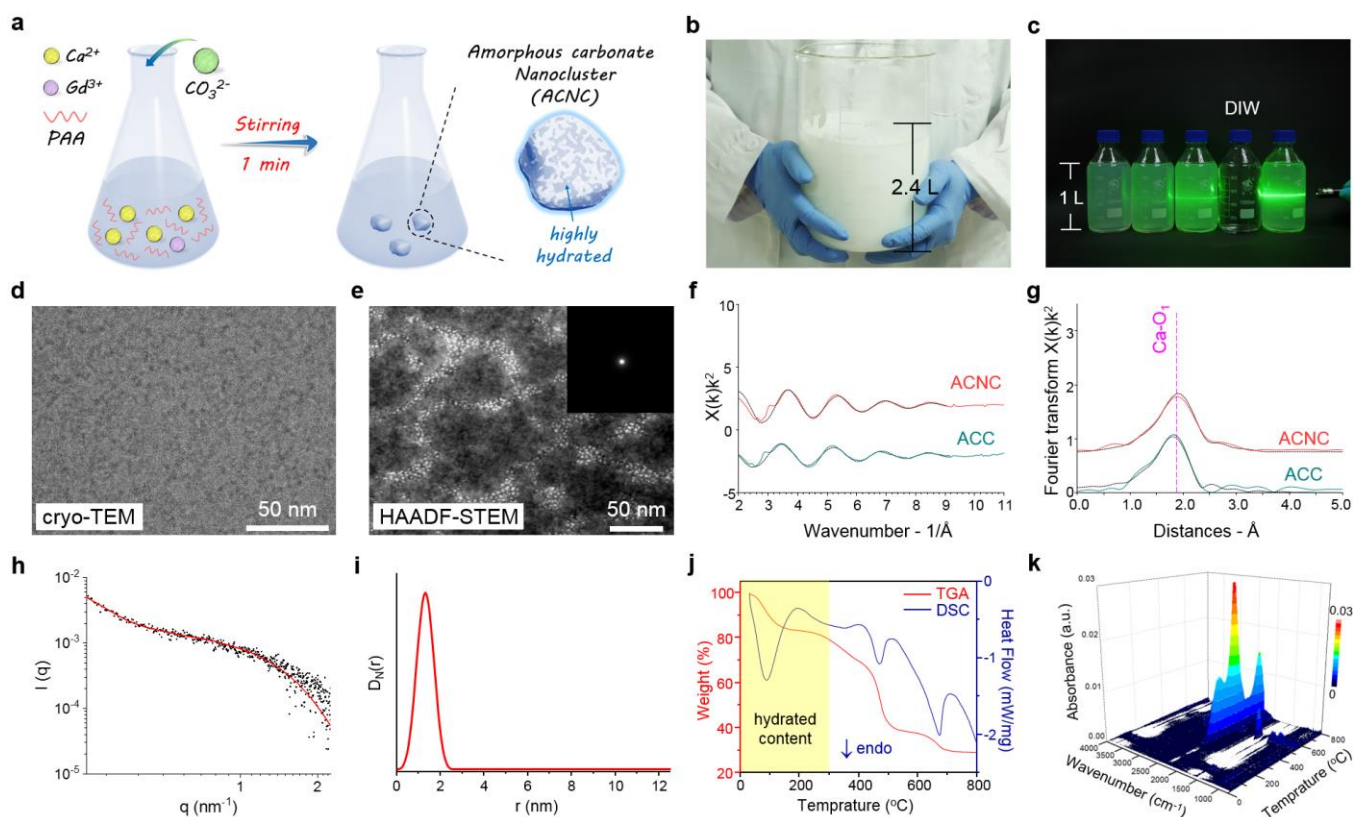
14 **Publisher's note:** Springer Nature remains neutral with regard to jurisdictional claims in published maps
15 and institutional affiliations.

16

17

1 **Figure Captions**

2



3

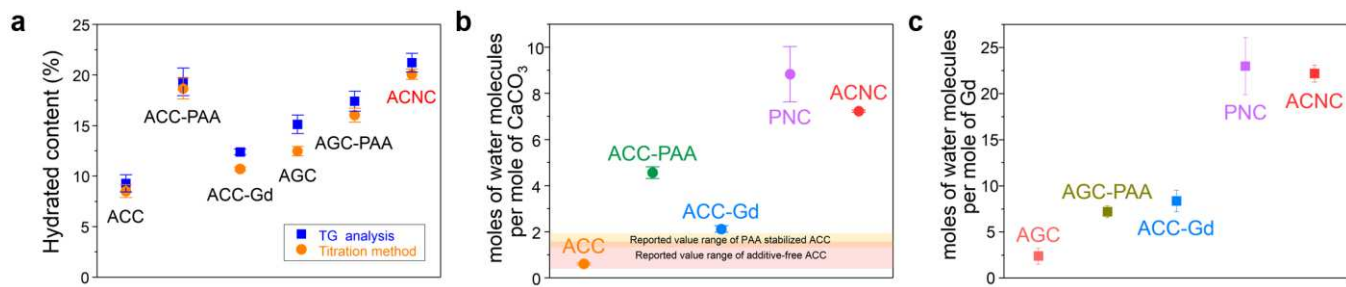
4 **Figure 1 | Characterization of amorphous carbonate nanocluster (ACNC).**

5 **a** Scheme of the synthesis process of ACNC. **b** Digital image of the large-scale prepared ACNC with the total volume over 2 litres.

6 **c** Digital image of Tyndall effect of four litres of ACNC dispersed in normal saline, and one bottle of deionized water was inserted (second from right). **d** cryo-TEM and **e** HAADF-STEM image of ACNC dispersed in normal saline solution. The inset in **e**, shows SAED of ACNC. **f** k^2 -weighted EXAFS and **g** k^2 -weighted Fourier transform of the EXAFS for the ACNC and ACC standard. Dotted black lines are their best fits. **h** SAXS patterns of ACNC dispersed in normal saline solution. Red solid line fit sphere particles. **i** Distance distribution received by SAXS of ACNC dispersed in normal saline solution. **j** TGA of ACNC powder under an N_2 atmosphere with a heating rate of $10\text{ }^\circ\text{C min}^{-1}$. **k** TG-FTIR spectra of ACNC powder under an N_2 atmosphere with a heating rate of $10\text{ }^\circ\text{C min}^{-1}$.

14

15



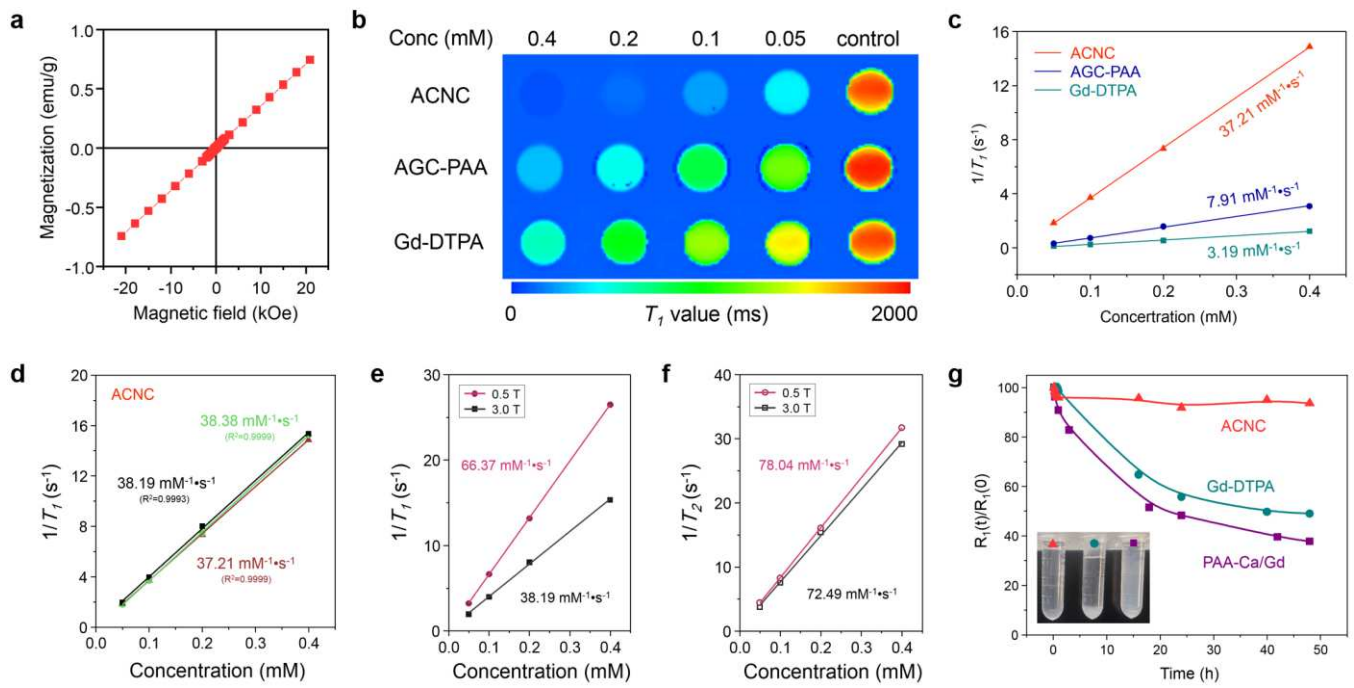
1

2 **Figure 2 | High water content of ACNC.** **a** The water contents of ACC, ACC-PAA, ACC-Gd, AGC,
 3 AGC-PAA and ACNC according to thermogravimetric (TG) analysis and volumetric Karl Fischer titration
 4 measurements. **b** Molar ratio of water molecules per mole of CaCO₃ in ACC, ACC-PAA, ACC-Gd and
 5 ACNC (n = 3) in comparison with the reported value ranges of additive-free ACC (pink region) and PAA-
 6 stabilized ACC (orange region). **c** Molar ratio of water molecules per mole of Gd in AGC, AGC-PAA,
 7 ACC-Gd and ACNC (n = 3).

8

9

10



1

2 **Figure 3 | MRI performance of ACNC. a** M-H curve of ACNC at room temperature. **b-c** T_1 map and

3 $1/T_1$ versus Gd concentration curve of ACNC ($R^2 = 0.9999$), AGC-PAA ($R^2 = 0.9987$) and Gd-DTPA (R^2

4 $= 0.9966$) under 3.0 T. **d** $1/T_1$ versus Gd concentration curve of ACNC under 3.0 T (n = 3). **e** $1/T_1$ versus

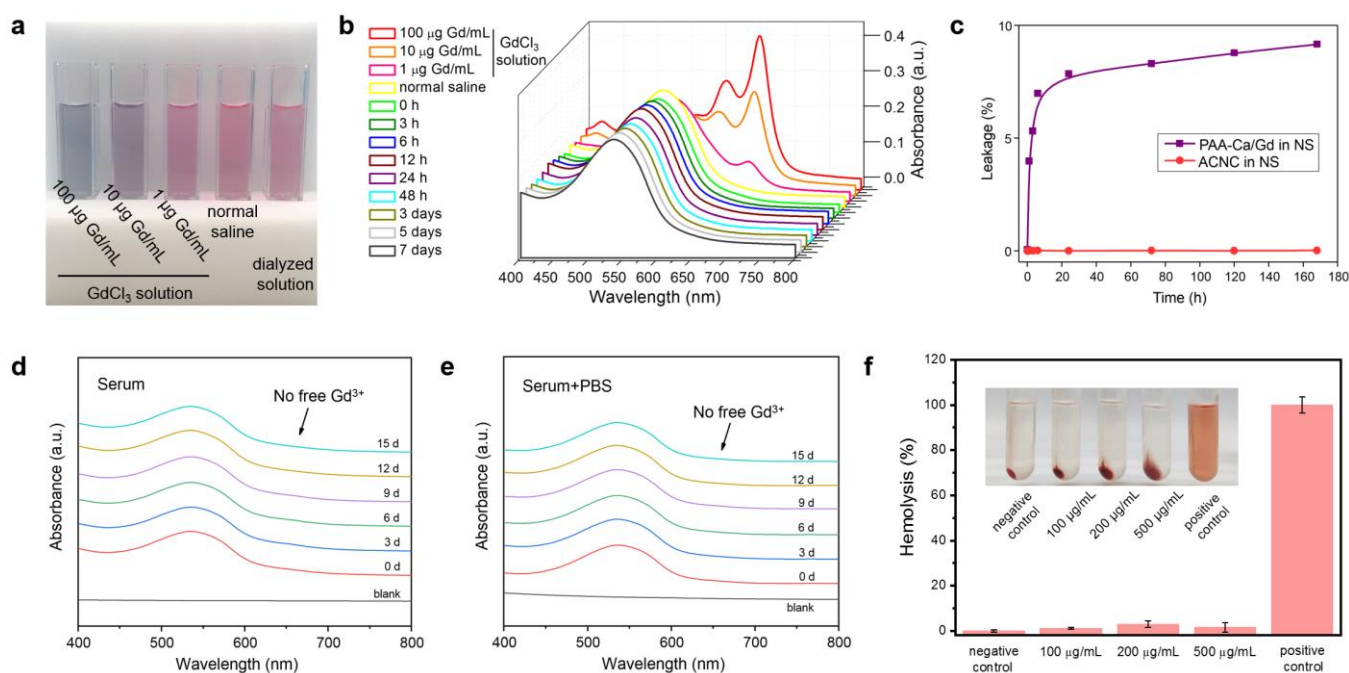
5 Gd concentration curve of ACNC under 3.0 T ($R^2 = 0.9993$) and 0.5 T ($R^2 = 0.9999$). **f** $1/T_2$ versus Gd

6 concentration curve of ACNC under 3.0 T ($R^2 = 0.9991$) and 0.5 T ($R^2 = 0.9999$). **g** Evolution of relative

7 R_1 values from the zero time to each time ($R_1(t)/R_1(0)$) for ACNC, Gd-DTPA and PAA-Ca/Gd.

8

9



1

2 **Figure 4 | Stability study.** **a** Photos of the mixtures of Arsenazo III aqueous solution with dialyzed

3 solutions of ACNC, normal saline (NS, served as negative control) and gadolinium chloride aqueous

4 solution at varying concentrations (1, 10 and 100 $\mu\text{g Gd/mL}$) (served as positive controls), respectively. **b**

5 Absorption spectra of arsenazo III-dialysate mixtures, and dialysates were collected at varying time points

6 in 7 days to monitor the leakage of gadolinium from ACNC. No detectable leakage of gadolinium ion was

7 monitored compared with the negative (NS) and positive (gadolinium chloride aqueous solution) controls.

8 **c** Quantitative analysis and comparison of the leakage of free gadolinium ion from ACNC and PAA-Ca/Gd

9 in NS by means of ICP-AES. PAA-Ca/Gd chelate showed poor inertness in NS, and approximately 9%

10 gadolinium was leaked from the chelate after 7 days. In contrary, few free gadolinium ion was detected in

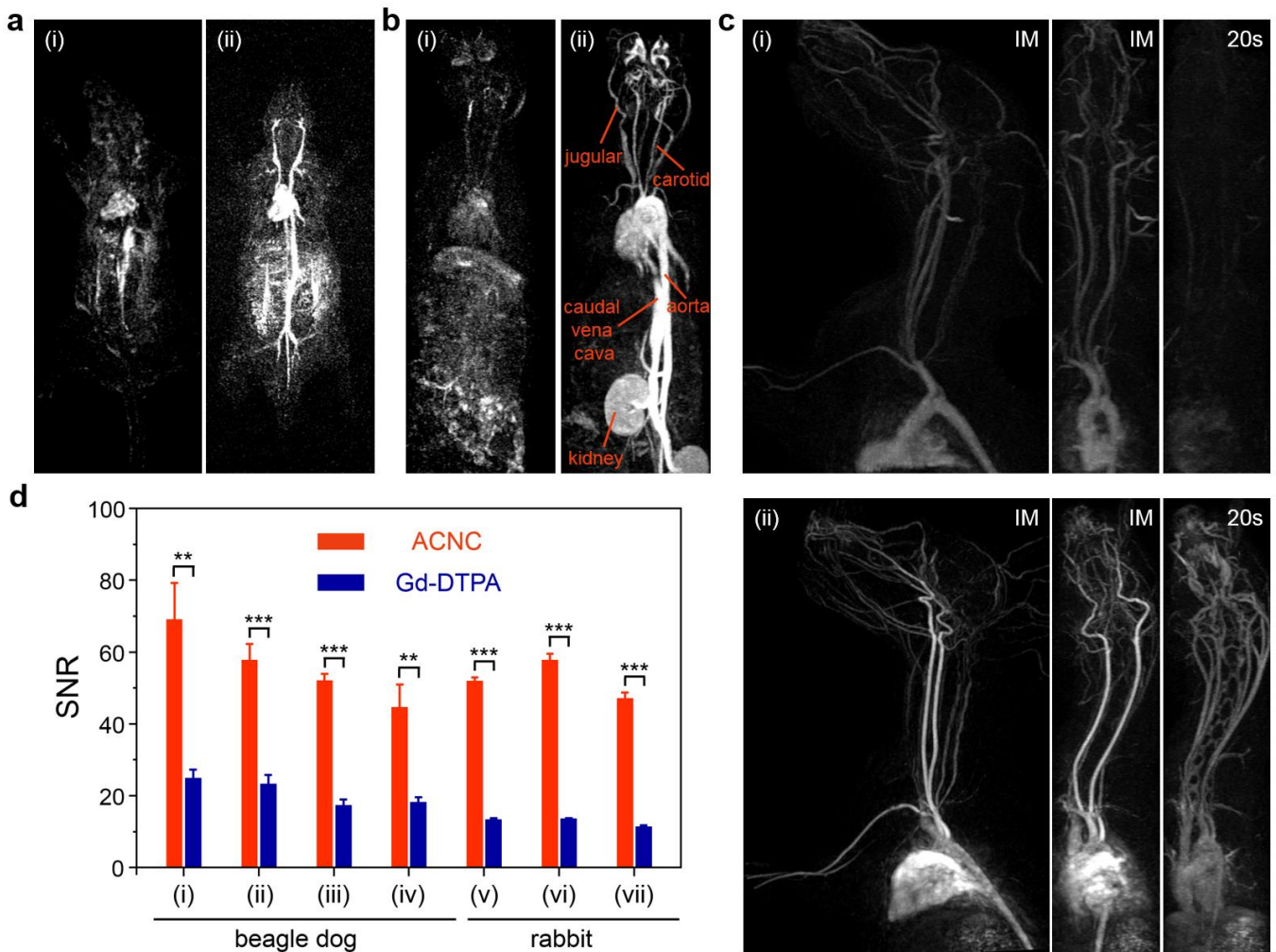
11 the dialysates of ACNC. **d-e** Absorption spectra of arsenazo III mixture with dialyzed solutions collected

12 at different time points from **d** human serum with dispersed ACNC and **e** human serum with dispersed

13 ACNC and supplemented additional phosphate. **f** Blood compatibility evaluation of ACNC at varying

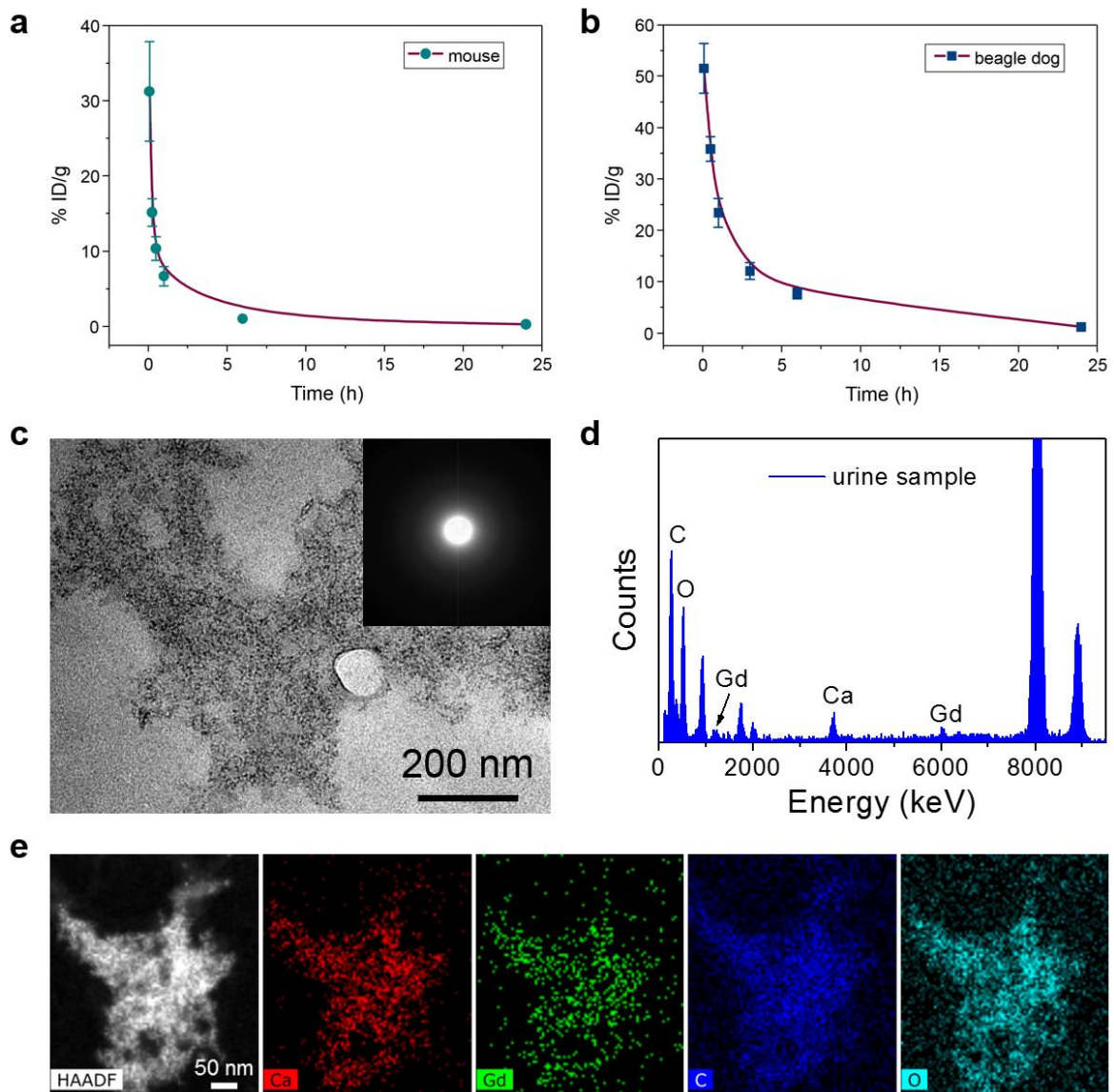
14 gadolinium concentration.

15



1
2 **Figure 5 | *In vivo* MR angiography. a-b** Contrast enhanced MR angiography (MRA) images of the whole
3 body on **a** rat and **b** rabbit immediately after the bolus injection of (i) Gd-DTPA and (ii) ACNC. **c** MRA
4 images of upper body on beagle dog at immediately (IM) and 20 seconds after the bolus injection of (i)
5 Gd-DTPA and (ii) ACNC, respectively. **d** Quantitative measurement of SNR of ROIs in (i) brachiocephalic
6 trunk artery, (ii) left subclavian artery, (iii) left common carotid artery, (iv) right branch of olfactory artery
7 of beagle dog, and that in (v) descending aorta, (vi) aortic arch, (vii) ascending aorta of rabbit, respectively.
8 The time for quantitative measurement of SNR of ROIs was in the “IM” period. (**P<0.01, ***P<0.001).

9
10



1
 2 **Figure 6 | Metabolism of ACNC. a-b** The time dependent distribution of ACNC in plasma of **a** mice and
 3 **b** beagle dogs within 24 hours. **c** TEM, **d** EDS results and **e** HAADF-STEM image and EDS mapping of
 4 ACNC observed in rat urine collected 12 hours post-injection. Inset of **c** is relative SAED pattern.

5

Supplementary Files

This is a list of supplementary files associated with this preprint. Click to download.

- [SupplementaryinformationACNCNatCommun.docx](#)